The crucial role of defect structure in understanding the electrical properties of spark plasma sintered antimony doped barium stannate

Materials Research Express

PAPER

The crucial role of defect structure in understanding the electrical properties of spark plasma sintered antimony doped barium stannate

Jelena Vukašinović[1,2,*], **Željko Rapljenović**[3,4], **Milica Počuča-Nešić**[1,2], **Tomislav Ivek**[3], **Zorica Branković**[1,2] and **Goran Branković**[1,2]

[1] University of Belgrade, Institute for Multidisciplinary Research, Kneza Višeslava 1a, 11030, Belgrade, Serbia
[2] University of Belgrade, Center of Excellence for Green Technologies, Institute for Multidisciplinary Research, , Kneza Višeslava 1a, 11030 Belgrade, Serbia
[3] Institute of Physics, Bijenička cesta 46, HR-10000, Zagreb, Croatia
[*] Author to whom any correspondence should be addressed.
[4] Present address: Institute for Nuclear Technology, INETEC, Dolenica 28, HR-10250 Zagreb, Croatia

E-mail: jelena.vukasinovic@imsi.bg.ac.rs

OPEN ACCESS

RECEIVED
7 December 2022

REVISED
12 January 2023

ACCEPTED FOR PUBLICATION
16 January 2023

PUBLISHED
25 January 2023

Keywords: barium stannate, spark plasma sintering, point defects, electrical resistivity, x-ray photoelectron spectroscopy

Abstract

The influence of structural defects in spark plasma sintered $BaSn_{1-x}Sb_xO_3$ (BSSO, $x = 0.00$ and 0.08) ceramic samples on their electrical properties was investigated in the temperature range of 300–4 K. X-ray photoelectron spectroscopy (XPS) revealed the presence of point defects, primarily oxygen vacancies (V_O) and mixed oxidation states of tin (Sn^{2+}/Sn^{4+}) in both samples. As a result, the undoped BSSO sample exibited a non-standard semiconductor behavior, retaining its temperature-dependent resistivity. The electrical resistivity of the doped samples was two orders of magnitude lower than that of the undoped sample. The presence of structural defects such as V_O, mixed oxidation states of the constituent elements, and significant amounts of O^- species make the electrical resistivity of the doped sample constant in the temperature range of 300–70 K, indicating heavily-doped semiconductor behavior.

1. Introduction

The modern industry shows a considerable demand for non-magnetic, non-inductive, and highly electroconductive materials that can work in conditions unfavorable for metals and alloys [1]. Performance and endurance of these materials in conditions of constant high voltage, current, and energy, with a particular emphasis on acidic and humid environmental conditions are also expected. Applying chemically inert and thermally stable ceramic resistors with linear current-voltage (*I-U*) characteristic, high energy, and a small resistivity temperature coefficient would satisfy the stated conditions [1]. For this purpose, the most suitable materials could be perovskite-type oxides with the general formula ABO_3 (A = alkaline Earth element; B = transition metal, O = oxygen). Appropriate doping into A and/or B sites can change perovskites' flexible structure and cause many structural modifications, *e.g.* lattice distortion and defect formation (cation and anion vacancies, grain boundaries), which significantly affect the materials' electrical properties [2–6].

In the materials preparation process, apart from doping, sintering conditions have a significant impact on electrical properties of final material. For example, sintering in the oxygen-poor atmosphere leads to the formation of oxygen vacancies as native intrinsic defects in ceramics, thus improving their electrical conductivity [7–10]. Spark plasma sintering (SPS) is a current and pressure assisted technique that takes place under vacuum conditions in a graphite die. The heating of the sample during the SPS process depends on both the electrical resistance of tool components and the electrical resistance of the sample material. During sintering of an insulating powder, at lower thermal treatment temperatures the current passes only through the graphite

die. However, as samples' electrical conductivity increases at higher temperatures, apart from the graphite die, the current starts to pass through the sample, *i.e.*, Joule heating in the sample occurs.

Contrary, in the case of highly doped conducting powder, the current passes directly through the sample, and Joule heating in the sample occurs even at low temperatures, whereby the heat is transmitted by the conduction to the powder. This sintering technique has a twofold effect on improving the electrical conductivity of ceramic materials. The first effect is related to the formation of oxygen vacancies in ceramic materials due to the reduction atmosphere during sintering process. The second one is related to the high current density flow through the sample with highly doped grains which have low potential barrier at grain boundaries. As a result, low angle grain boundaries (LAGBs) are formed, causing complete loss of the potential barrier at grain boundaries [9].

Barium stannate ($BaSnO_3$, BSO), a perovskite-type alkaline Earth stannate, is distinguished among other perovskite oxides by its ideal cubic crystal structure (space group: $Pm\bar{3}m$), Goldschmidt factor close to 1 [11], thermal stability up to 1000 °C, non-toxicity and easy methods of preparation [4, 5, 12, 13]. Its crystal structure consists of Ba^{2+} ions on the corners of the cube, with each Ba^{2+} ion coordinated by twelve O^{2-} ions forming cubic close-packed lattice, while Sn^{4+} ions are occupying octahedral holes created by O^{2-} ions [13, 14]. Undoped BSO exhibits semiconductor-like behavior with wide band gap in the range of 3.1–3.4 eV [3, 4, 12, 13, 15–19], which can be modified by careful replacement of Ba^{2+} or/and Sn^{4+} with aliovalent cations [3–6, 13, 15]. In dependence on the dopant type and concentration, BSO can show n-type semiconductor behavior, as well as metallic-like conductivity similar to some heavily-doped semiconductors [3, 4, 18, 20–22]. Based on literature data, the replacement of tin by antimony can increase the mobility and charge carrier density, thus improving the electrical conductivity of BSO ceramics [2–5, 15, 16, 19, 23, 24].

In our previous work we reported on the influence of Sb-doping on properties of spark plasma sintered BSO [25]. Among all presented ceramic samples, the one with composition $BaSn_{0.92}Sb_{0.08}O_3$ stood out, having linear *I-U* characteristic and stable electrical conductivity in the temperature range of 25 °C–150 °C. Its metallic-like behavior was ascribed to the loss of potential barrier at the grain boundary region due to the low angle grain boundaries present only in this sample. Even though the negative value of the Hall coefficient confirmed n-type conductivity in $BaSn_{0.92}Sb_{0.08}O_3$ ceramic sample, suggesting the substitution of Sn^{4+} with Sb^{5+}, we cannot completely dismiss the assumption that the Sb^{3+} is also present in the sample, even in small concentrations. Apart from antimony, tin as a host ion can also exist in different oxidation states. Combination of sintering conditions and the volatile nature of tin could result in the reduction of Sn^{4+} into Sn^{2+}, or even to metallic Sn. As stated before, SPS favors the creation of oxygen vacancies [7–10, 26–28], which behave as electron donors and improve the materials electrical conductivity with a maximum of two electrons (per vacancy) [5, 6, 15–17, 29]. Compared to other intrinsic defects formed under poor oxygen conditions, they have the lowest formation energy, and their presence is the most expected in BSSO samples. Apart from LAGBs and Vo, many point defects such as Sn^{2+}, Sn^{4+}, Sn^0, Sb^{3+} and Sb^{5+}, as well as ionized and neutral impurities originating from antimony doping and sintering conditions can also exist in BSSO ceramics [5, 13, 15, 19, 29].

The aim of this work was to clarify the striking change from semiconductor-like ($BaSnO_3$) to metallic-like ($BaSn_{0.92}Sb_{0.08}O_3$) electrical properties of spark plasma sintered ceramics. For this purpose we performed a broad investigation of materials defect structure and electrical properties using x-ray powder diffraction (XRD), X-ray photoelectron spectroscopy (XPS), Secondary ion mass spectrometry (SIMS) analyses and four probe electrical measurements.

2. Experimental procedure

The preparation of precursor powders and ceramic samples of $BaSn_{1-x}Sb_xO_3$ ($x = 0.00$ and 0.08), the conditions of XRD analysis and the method for determination of the average grain size were described in our previous paper [25]. Using the value of the unit cell parameter for the BSSO0 sample calculated by *PowderCell* and *LSUCRI* software, the structural model of cubic $BaSnO_3$ was constructed using *CrystalMaker* software. Subsequently, in the same software the Sn–O and Ba–O bond lengths were calculated, as well as the value of Sn–O–Sn bond angle in both BSSO samples. In dependence of antimony concentration, in this paper samples are denoted as BSSO0 ($BaSnO_3$, $x = 0.00$) and BSSO8 ($BaSn_{0.92}Sb_{0.08}O_3$, $x = 0.08$).

The XPS analysis was carried out in a SPECS instrument equipped with a Phoibos MCD 100 electron analyzer and a monochromatized source of Al Kα x-rays of 1486.74 eV. The binding energy (BE) scale of XPS spectra was calibrated by the reference carbon C 1s peak, adjusted to the BE of 285.0 eV. The experimental curves were deconvoluted with Pseudo-Voigt profiles using the *Python* program [30].

The experimental conditions of spark plasma sintering using high temperature and high pressure in vacuum atmosphere can cause the evaporation of antimony and the formation of oxide layers on the surface of both

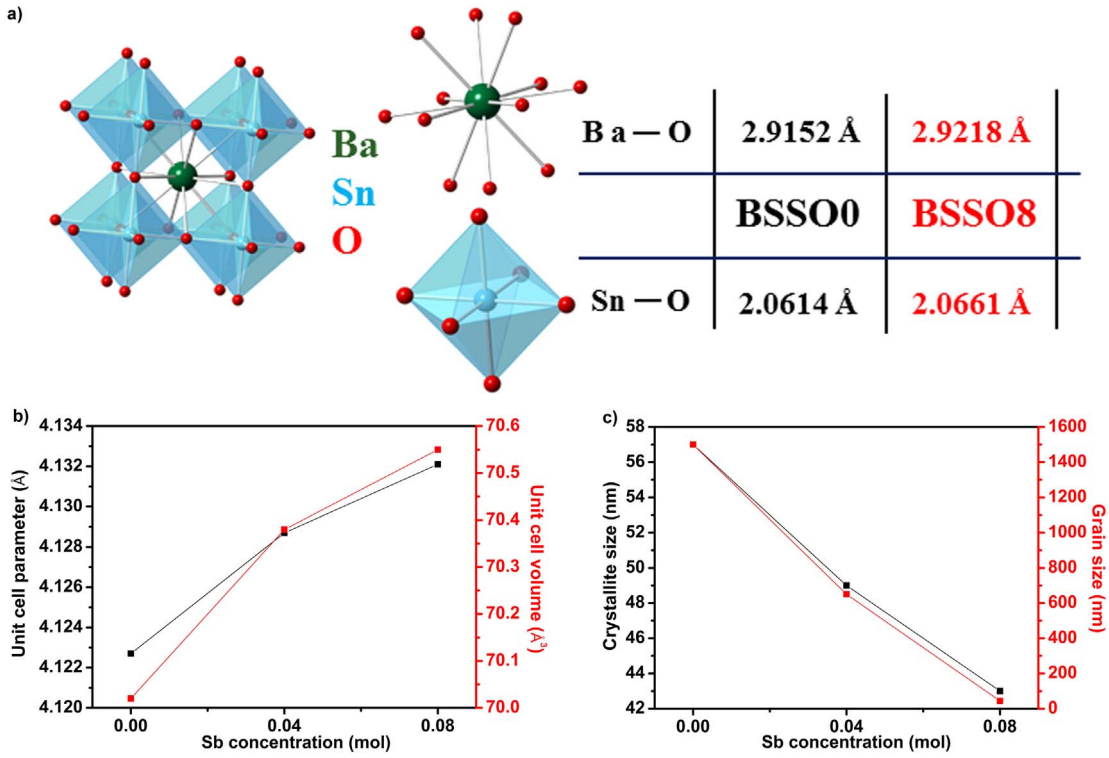

Figure 1. (a) The cubic perovskite crystal structure of $BaSnO_3$ constructed by CrystalMaker software (green sphere—Ba ions, blue sphere—tin ions, and small red sphere—oxygen ions), table: Ba–O and Sn–O bond lengths for both BSSO samples; (b) The dependence of the unit cell parameter and unit cell volume of the Sb concentration; (c) The dependence of the crystallite and grain size of the Sb concentration in BSSO samples ($x = 0.00$, 0.04, and 0.08).

BSSO ceramic samples. For this reason, the surface of the BSSO samples was cleaned by the low energy Ar^+ ion sputtering to remove the topmost layer of the material.

A Hiden SIMS workstation, equipped with the quadruple mass analyzer, was employed for the SIMS measurements, where the bombardment with 3 keV O_2^+ primary ions at an impact angle of 45° was used for the collection of positive secondary ions.

Electrical characterization of BSSO0 and BSSO8 ceramic samples has been performed in the temperature range from room temperature to liquid helium temperature (300–4 K). The current was provided using the Keithley 6221 current source and the voltage was measured using Keithley 2182A nanovoltmeter. The electrical contacts were painted using the conductive silver paint DuPont 4929N in linear 4-probe configuration.

3. Results and discussion

3.1. Structural analyses

3.1.1. XRD analysis

XRD analysis revealed that the dominant phase in both samples is cubic $BaSnO_3$[25]. The amount of secondary phase, Ba_2SnO_4, decreased upon doping with Sb from 15 to 8% for BSSO0 and BSSO8, respectively [25]. Figure 1(a) presents the structural model of cubic BSSO constructed by *CrystalMaker* software using the value of the unit cell parameter previously obtained by *PowderCell* and *LSUCRI* software [25]. It also shows that doping with antimony induces the changes in the crystal lattice of BSO, leading to the increase of Sn–O and Ba–O bond lengths in the doped BSSO8 sample. (figure 1(a), (Inset table). Although these changes are small, they have a significant influence on structural, microstructural, and especially on electrical properties of Sb-doped sample (Electrical properties, section 3.2). The value of the Sn–O–Sn bond angle is 180° and is identical for both analyzed samples.

Figure 1b shows the dependence of the unit cell parameter on the dopant concentration, with obvious expansion of the unit cell upon doping. Since the BSSO ceramic samples were prepared in vacuum atmosphere, the presence of oxygen vacancies in both BSSO samples is expected. These defects can induce the increase of the unit cell parameter through the increase of electrostatic repulsion between Sn and Ba cations [16]. The more pronounced expansion of the unit cell parameter in the BSSO8 sample is caused by a joint effect of doping and sintering conditions: incorporation of Sb^{3+} ions on the Sn^{4+} sites and stronger Coulomb repulsion between

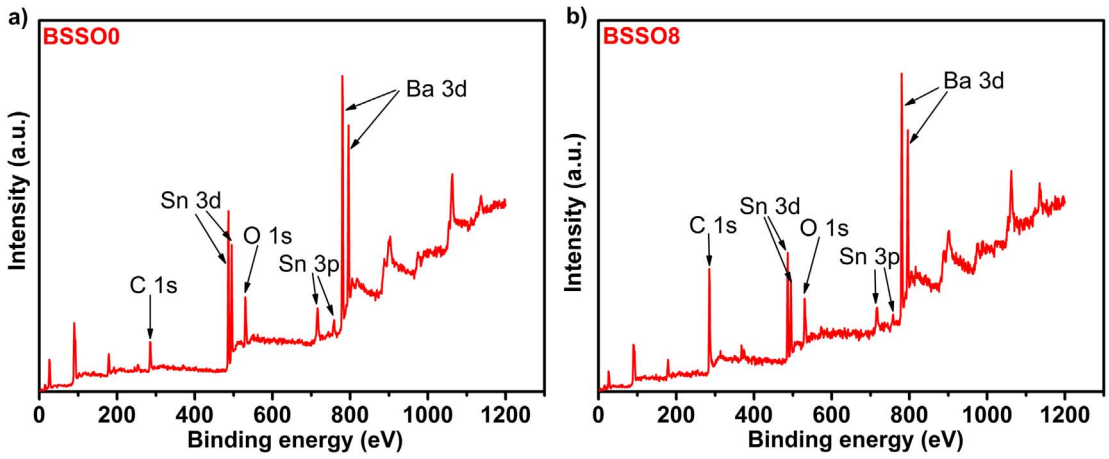

Figure 2. The survey XPS spectra for the: (a) BSSO0 and (b) BSSO8 samples after Ar ion. sputtering.

Ba^{2+} and cations with mixed-valence states (Sn^{2+}/Sn^{4+} and Sb^{3+}/Sb^{5+}). Doping with Sb decreases both crystallite and grain sizes, resulting in almost identical values of these parameters for the BSSO8 sample, ~43 nm (figure 1(c)).

3.1.2. XPS analysis

The survey of XPS spectra (figures 2(a) and (b), respectively) confirmed the presence of Ba, Sn and O in of BSSO0 and BSSO8 samples. Recorded spectra have been measured after Ar ion sputtering, with the intent of eliminating uncoordinated oxide layers formed on the surface, as well as the possible carbon contamination as a result of the sample handling. According to the literature data, the inert noble gas does not change the chemistry of the surface but it can be incorporated in the structure [31].

The presence of Sb was not detected in the survey XPS spectra of BSSO8 after cleaning of the surface with the Ar ions. This apparent lack of Sb could be limited only to the samples surface, since XPS is a surface sensitive technique, probing only a few layers of material.

XPS spectra of Ba 3d core level for BSSO0 and BSSO8 samples show a spin–orbit doublet structure (figures 3(a) and (b)), corresponding to the $3d_{5/2}$ and $3d_{3/2}$ states of Ba. A spin–orbit splitting of 15.3 eV and 15.4 eV confirms the presence of Ba^{2+} [32–34] in both BSSO0 and BSSO8 samples, respectively.

In the case of BSSO0 sample, the Ba peak of $3d_{5/2}$ core level was fitted by a single Pseudo-Voigt profile centered at 780.5 eV (figure 3(c)), while for the BSSO8 sample the same peak is broader and deconvoluted into two components centered at 780.5 eV and 782.4 eV, (figure 3(d)). Low energy component with binding energy of 780.5 eV corresponds to Ba^{2+} ions. The high energy broad peak has already been reported in the perovskite materials, but its origin was left undiscussed [35]. We assume that high energy Ba $3d_{5/2}$ peak originates from the defects formed in BSSO crystal lattice upon Sb doping. These defects could induce drastic changes in Ba–O bonds resulting in a new component centered at 782.4 eV.

The binding energies of the Sn $3d_{5/2}$ core level in three oxidation states Sn^0, Sn^{2+} and Sn^{4+} can be observed at 485.0 eV, 485.9 eV and 486.6 eV, respectively [21]. The spin–orbit splitting (figures 4(a) and (b)), after Ar ion sputtering is about 8.4 eV and 8.5 eV for the BSSO0 and BSSO8, respectively, confirming the existence of Sn^{4+} [5, 19, 34, 36].

In the case of Sn spectra of BSSO0 sample (figure 4(c)), the peak of $3d_{5/2}$ core level was fitted by two components centered at 485.8 eV and 486.7 eV, corresponding to the Sn^{2+} and Sn^{4+} states, respectively. Identical components, regarding energy were observed in BSSO8 sample, but with different relative integrated intensity (figure 4(d)).

Spark plasma sintering performed in a vacuum atmosphere at temperatures above 600 °C can lead to a reaction between carbon from the graphite mold (and possibly from foil) with oxygen form the sample. This process decreases the oxygen partial pressure, resulting in the formation of CO, oxygen vacancies and reduction atmosphere in the reaction system. Consequently, we could expect the reduction of some amount of Sn^{4+} into Sn^{2+} or even metallic Sn, which was already proven in our previous paper [25]. However, the presence of the metallic tin was not detected in any sample, since the topmost layers containing it were removed during the Ar ion sputtering.

In both BSSO0 and BSSO8, relative quantity of Sn^{2+} was calculated from the ratio of integrated intensity of components Sn^{2+}/Sn^{4+}. The BSSO0 sample has 5.8% of Sn^{2+} of the total amount of tin, while BSSO8 sample

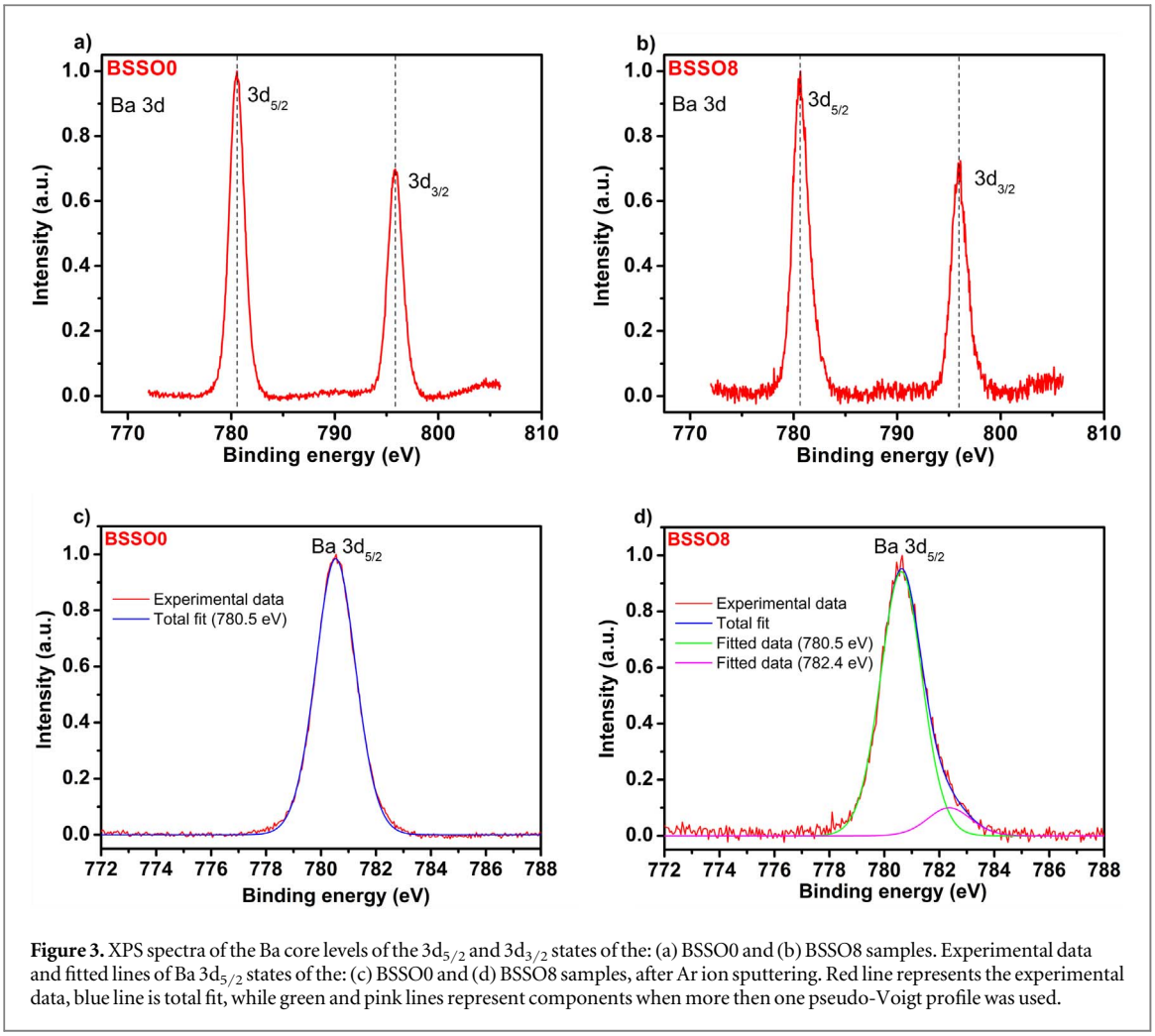

Figure 3. XPS spectra of the Ba core levels of the $3d_{5/2}$ and $3d_{3/2}$ states of the: (a) BSSO0 and (b) BSSO8 samples. Experimental data and fitted lines of Ba $3d_{5/2}$ states of the: (c) BSSO0 and (d) BSSO8 samples, after Ar ion sputtering. Red line represents the experimental data, blue line is total fit, while green and pink lines represent components when more then one pseudo-Voigt profile was used.

has only 0.5% of bivalent tin. This indicates that the incorporation of antimony in BSO matrix stabilizes the perovskite structure. This stabilization is reflected in the decrease of the secondary phase content in this sample, uniformity of its grain size distribution and the overall reduction of the grain size, which in BSSO8 is approximately equal to crystallite size (figure 1(c)).

The O 1s spectra (shown on figures 5(a) and (b)) of both samples show a broad and highly asymmetric structure. The spectrum of BSSO0 sample is deconvoluted into two components one at 530.2 eV and 531.9 eV, while for the BSSO8 the component energies are 530.3 eV and 532.5 eV. The low energy component for both samples is associated with the presence of O^{2-} oxygen species, commonly referred to as lattice oxygen [5, 18, 32]. The higher energy peak is associated with O^{-} species in both samples disregarding the 0.6 eV shift. The exact origin of the O^{-} species is not clear [37]. Sometimes high energy peaks are correlated to the presence of the oxygen vacancies and oxygen species adsorbed on the samples surface [18, 19, 32, 33].

We present here our hypothesis for the origin of the O^{-} species which can be correlated with the structural properties. We presume that the oxygen in the ceramic samples exists at least in two different environments, first coordinated oxygen in the crystal lattice (O^{2-}) and the second one, O^{-}, either the surface oxygen or the grain boundary oxygen. This hypothesis fits well with our data, because BSSO8 has smaller grain size and lower density which implies higher concentration of grain boundaries and surfaces which further implies more O^{-} species in this sample.

Relative percentage of integrated intensity of the deconvoluted components (O^{2-} and O^{-} species) in BSSO0 sample is 60.0% and 40.0% while in the BSSO8 sample is 52.1% and 47.9%, respectively.

3.1.3. SIMS analysis

During the XPS measurements, to the best of our attempts, we could not find clear evidence of electrons ejected from Sb core levels in the doped sample. We here stress that considerable amount of time has passed between the sample preparation and the XPS measurements, and that during this period surface Sb has diffused out from the topmost layers. Taking this reasoning into account, we examined the presence of antimony in bulk and on the samples surface using SIMS analysis for it is more sensitive technique for elemental analysis. Antimony in its

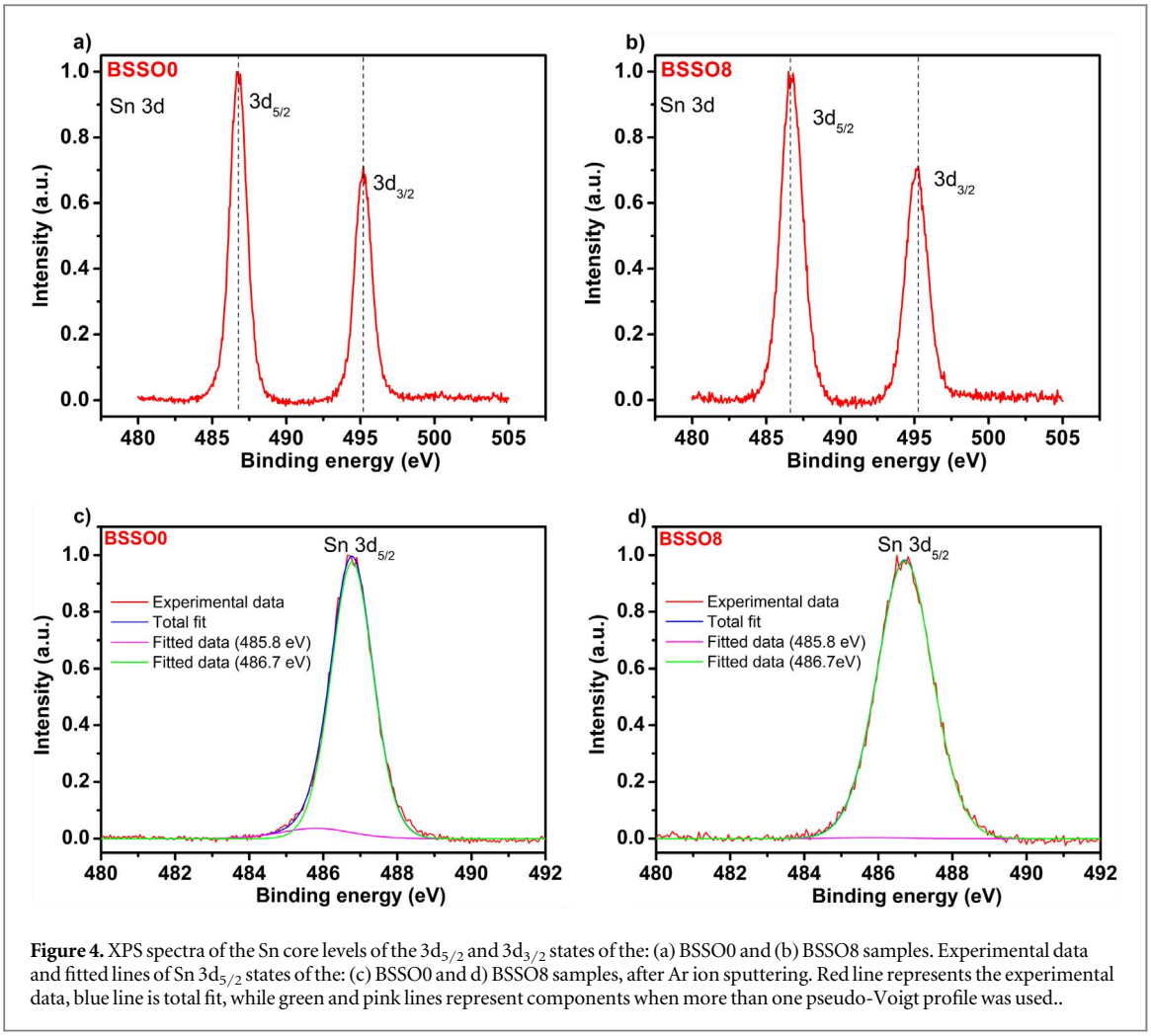

Figure 4. XPS spectra of the Sn core levels of the $3d_{5/2}$ and $3d_{3/2}$ states of the: (a) BSSO0 and (b) BSSO8 samples. Experimental data and fitted lines of Sn $3d_{5/2}$ states of the: (c) BSSO0 and d) BSSO8 samples, after Ar ion sputtering. Red line represents the experimental data, blue line is total fit, while green and pink lines represent components when more than one pseudo-Voigt profile was used..

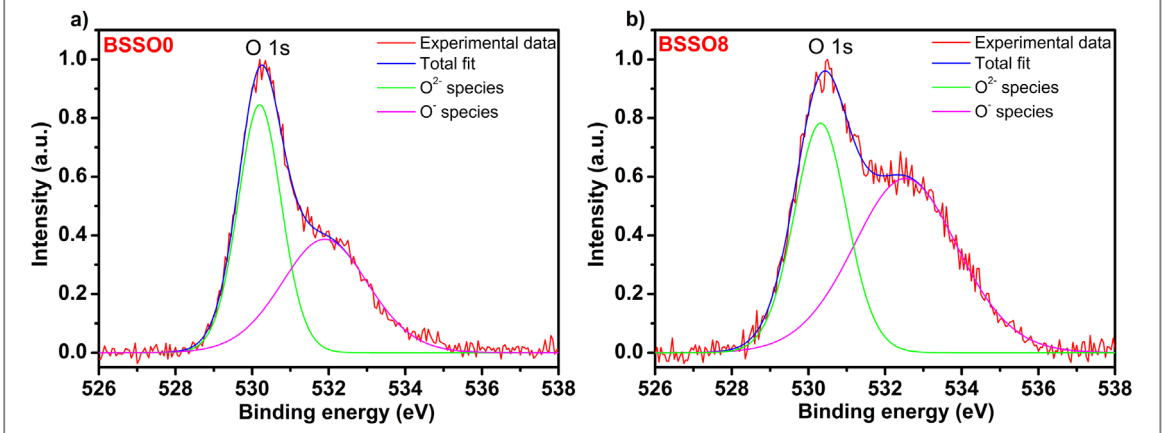

Figure 5. XPS spectra of O 1s core level of the: (a) BSSO0 and (b) BSSO8 samples, after Ar ion sputtering. Red line represents the experimental data, blue line is total fit, while green and pink lines are deconvoluted components (O^{2-} and O^{-} species), respectively.

pure state has two isotopes with mass of 121 and 123 atomic mass units (a.m.u.) [38, 39]. As expected, the SIMS spectrum of BSSO0 shows no presence of antimony in the sample (figure 6(a)). The small intensity at mass 121 is probably due to molecules and/or clusters of residual Silver (109 a.m.u.) whose origin is from the silver paste used for electrical contacts and adsorbed Carbon (12 a.m.u.). From SIMS spectrum of the BSSO8 sample (figure 6(b)), we can see a high intensity at masses 121 and 123 which confirms the presence and stability of antimony in the bulk.

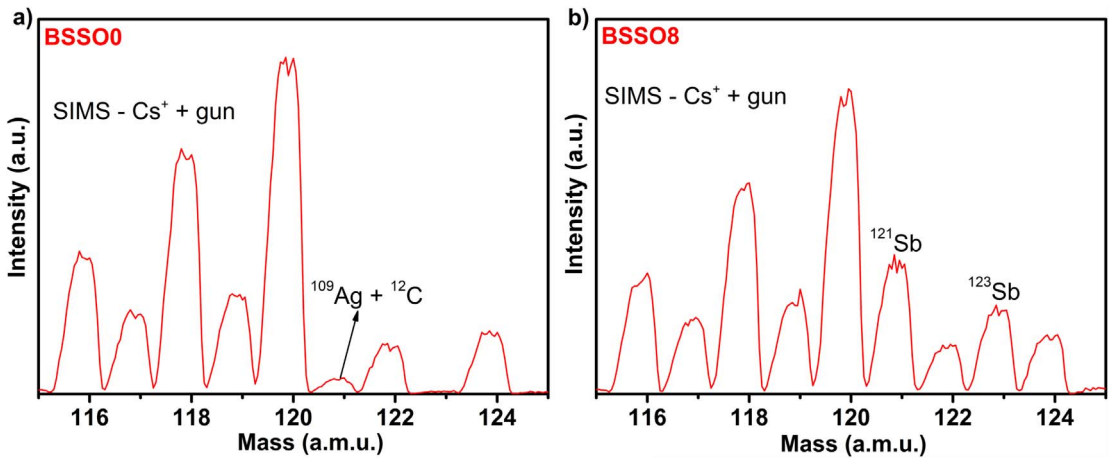

Figure 6. SIMS spectra of the: (a) BSSO0 and (b) BSSO8 ceramic samples, near Sb isotopes.

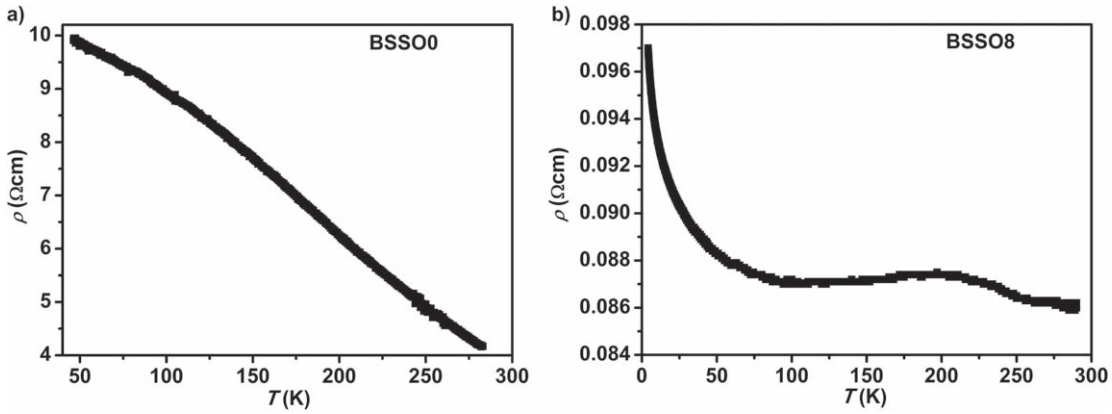

Figure 7. Temperature dependence of resistivity of the: (a) BSSO0 and (b) BSSO8 ceramic samples.

3.2. Electrical properties

Previously, the temperature dependence of electrical resistivity of BSSO ceramic samples was investigated in the range 25 °C–150 °C in the air atmosphere. The undoped sample showed the typical semiconductor behavior, while the BSSO8 sample showed almost temperature-independent resistivity. Since both BSSO samples revealed n-type conductivity we could conclude that dominant charge carriers are electrons originating from the presence of oxygen vacancies and the dopant [25].

This work covers the precise investigation of the electrical properties of BSSO0 and BSSO8 ceramic samples in a different temperature range, from room temperature to liquid helium temperature, using four-point probe method to exclude the influence of contacts and wires.

In the case of BSSO0 sample (figure 7(a)), it can be seen that the electrical resistivity decreases with the increase of temperature. Taking into account that the oxygen vacancies are the most common intrinsic defects in perovskites, we could assume that their presence increased electrical conductivity of the undoped BSSO0 sample, resulting in the suppression of standard activated semiconductor behavior while retaining resistivity which increases with cooling. The experimental results below 50 K are excluded from the plot due to observed electrical noise and consequently their low reliability.

In polycrystalline semiconductor samples, the conductivity is closely related to the scattering processes at the grain boundaries, and can be reduced by trapping the charge carriers at the electrostatic barrier [40, 41]. These processes are temperature dependent. In the case of BSSO0 sample, intrinsically doped by oxygen vacancies, the shown temperature-dependent resistivity (figure 7(a)) is a result of mentioned scattering process, but primarily of the enhancement of charge carriers' concentration with temperature.

In the case of BSSO8 sample, the electrical resistivity (figure 7(b)) is two orders of magnitude lower than in the BSSO0 sample. It is almost constant in the examined temperature range, with a distinct plateau from 70 K to 300 K and only a 10% change at temperatures below 70 K. A similar behavior was noticed in the case of heavily-

doped semiconductors, where the high dopant concentration reduces the electrostatic barriers related to grain boundaries, allowing unimpeded electron transport [41]. Also, Hossain and coworkers reported that change from the semiconductor to metallic-like behavior of Sb-doped BSO occurs at dopant concentration higher than 12.5% [42]. The unusual transport properties of BSSO8 are likely the consequence of mixed oxidation states of Sn^{2+}/Sn^{4+}, probably mixed states of Sb^{3+}/Sb^{5+}, as well as the presence of the high content of the O^{-} species, which shift up the Fermi level very close to or into the conduction band. In this sample, all charge carriers originating from extrinsic ionized defects are apparently excited in the whole measured temperature range, resulting in an almost temperature-independent resistivity. Further, the excitation of electrons from the deeper states in the BSSO8 sample does not significantly increase the concentration of charge carriers.

The low value of resistivity is also the result of limited grain boundary scattering since this process is significantly lowered in BSSO8 sample due to the presence of large fraction of LAGBs, whose formation is favored by high concentration of charge carriers together with spark plasma sintering conditions [10]. Therefore, a large fraction of LAGBs formed in BSSO8 sample led to a complete loss of potential barriers, as described in our previous work [25].

Keeping in mind the linear *I-U* characteristic of the BSSO8 sample [25] and high concentration of structural defects *i.e.* Sn^{2+}/Sn^{4+}, O^{-} species, probably Sb^{3+}/Sb^{5+} and LAGBs, as well as the free charge carrier transport through the grain boundaries, the diverse application of this ceramic material can be expected. Hence, spark plasma sintering of these heavily-doped semiconductors could be the key to satisfy the growing demand for moderate or high conductivity resistors with almost constant electrical resistivity in the wide temperature range. They can be used in cases that especially require non-magnetic, chemically inert and thermally stable resistors, which have high power density and high conductivity at lower temperatures.

4. Conclusions

This work correlates the type and quantity of defects in spark plasma sintered Sb-doped barium stannate with the striking change of its electrical properties from semiconductor in $BaSnO_3$ to metallic-like in $BaSn_{0.92}Sb_{0.08}O_3$.

The oxygen deficient sintering conditions caused the reduction of certain amount of Sn^{4+} to Sn^{2+} in both samples, whereby the charge compensation was realized through the formation of structural defects in both BSSO samples. The oxygen vacancies improved the electrical conductivity of BSSO0 sample, with absence of standard activated semiconductor behavior, but retaining temperature-dependent resistivity in the examined range. Doping with antimony increased unit cell parameter and at the same time stabilized the perovskite BSO crystal structure by reducing the content of Sn^{2+} in BSSO8 sample. The synergetic effect of Sb-doping and sintering conditions induced the formation of many structural defects, including LAGBs in the BSSO8 sample, which significantly decreased its electrical resistance and made it behave like a heavily doped semiconductor.

Acknowledgments

The authors acknowledge financial support of Ministry of Education, Science, and Technological Development of Republic of Serbia (Contract No. 451–03–68/2022–14/200053). Ž Rapljenović and T Ivek acknowledge the support of Croatian Science Foundation project IP-2018–01–2730 and of project Cryogenic Centre at the Institute of Physics - KaCIF co-financed by the Croatian Government and the European Union through the European Regional Development Fund-Competitiveness and Cohesion Operational Programme (Grant No. KK.01.1.1.02.0012). This work was done as a part of the cooperation between Institute for Multidisciplinary Research (University of Belgrade, Belgrade, Serbia), Institute of Physics (Zagreb, Croatia) and Department of Physics and Center for Micro and Nanosciences and Technologies (University of Rijeka, Rijeka, Croatia). The authors owe special thanks to Robert Peter (Department of Physics and Center for Micro and Nanosciences and Technologies, University of Rijeka, Rijeka, Croatia) for providing access to devices for SIMS and XPS analyses, as well as helpful tips and instructions during the processing of these results. T Ivek thanks Matija Čulo (Institute of Physics, Zagreb, Croatia) for elucidating discussions.

Data availability statement

The data generated and/or analysed during the current study are not publicly available for legal/ethical reasons but are available from the corresponding author on reasonable request.

Conflicts of interest

The authors declare no conflict of interest.

Statement on ethics approval

This study did not involve human and animal subjects.

ORCID iDs

Jelena Vukašinović https://orcid.org/0000-0002-7372-4064
Željko Rapljenović https://orcid.org/0000-0002-8237-5548

References

[1] Chen X, Li G, Tian T, Ruan X, Zheng L, Makowska-Janusik M, Rousseau A and Kassiba A 2022 Microstructural and electrical features of highly conducting indium co-doped ZnO-based ceramics *J. Am. Ceram. Soc.* **105** 1–13
[2] Scanlon D O 2013 Defect engineering of $BaSnO_3$ for high-performance transparent conducting oxide applications *Phys. Rev. B* **87** 161201 (R)
[3] Mizoguchi H, Chen P, Boolchand P, Ksenofontov V, Felser C, Barnes P W and Woodward P M 2013 Electrical and optical properties of Sb-doped $BaSnO_3$ *Chem. Mater.* **25** 3858–66
[4] Liu Q, Dai J, Liu Z, Zhang X, Zhu G and Ding G 2010 Electrical and optical properties of Sb-doped $BaSnO_3$ epitaxial films grown by pulsed laser deposition *J. Phys. D: Appl. Phys.* **43** 455401
[5] Sarkar A and De S K 2018 Defect and optical properties of Sb doped and hydrogenated $BaSnO_3$ *Semicond. Sci. Technol.* **33** 035018
[6] Singh P, Brandenburg B J, Sebastian C P, Singh P, Singh S, Kumar D and Parkash O 2008 Electronic structure, electrical and dielectric properties of $BaSnO_3$ below 300 K *Jpn. J. Appl. Phys.* **47** 3540–5
[7] Licheri R, Fadda S, Orrù R, Cao G and Buscaglia V 2007 Self-propagating high-temperature synthesis of barium titanate and subsequent densification by spark plasma sintering (SPS) *J. Eur. Ceram. Soc.* **27** 2245–53
[8] Kim Y, Watanabe M, Takagaki A, Matsuda J and Ishihara T 2019 Spark plasma sintering treatment for introduction of oxygen vacancy in Pt dispersed $SrTiO_3$ for increasing photocatalytic water splitting activity *ChemCatChem* **11** 1–6
[9] Guillon O, Gonzalez-Julian J, Dargatz B, Kessel T, Schierning G, Räthel J and Herrmann M 2014 Field-assisted sintering technology/spark plasma sintering: mechanisms, materials, and technology developments *Adv. Eng. Mater.* **16** 830–49
[10] Chaim R, Chevallier G, Weibel A and Estournès C 2018 Grain growth during spark plasma and flash sintering of ceramic nanoparticles: a review *J. Mater. Sci.* **53** 3087–105
[11] Bévillon É, Chesnaud A, Wang Y, Dezanneau G and Geneste G 2008 Theoretical and experimental study of the structural, dynamical and dielectric properties of perovskite $BaSnO_3$ *J. Phys. Condens. Matter* **20** 145217
[12] John J, Chalana S R, Mahadevan Pillai V P, Joseph J, Muthunatesan S, Ragavendran V and Tiwari G 2020 Characterization and optical limiting behavior of $BaSnO_3$ powder prepared by the conventional solid state method *Mater. Today Proc.* **29** 1091–7
[13] Wei R, Tang X, Hu L, Luo X, Yang J, Song W, Dai J, Zhu X and Sun Y 2018 Growth, microstructures, and optoelectronic properties of epitaxial $BaSn_{1-x}Sb_xO_{3-\delta}$ thin films by chemical solution deposition *ACS Appl. Energy Mater.* **1** 1585–93
[14] Ochoa-Muñoz Y H, Rodríguez-Páez J E and Mejía de Gutíerrez R 2021 Structural and optical study of perovskite nanoparticles $MSnO_3$ (M = Ba, Zn, Ca) obtained by a wet chemical route *Mater. Chem. Phys.* **266** 124557
[15] Kim H J *et al* 2013 Indications of strong neutral impurity scattering in $Ba(Sn,Sb)O_3$ single crystals *Phys. Rev. B* **88** 125204
[16] Liu Q, Dai J, Zhang Y, Li H, Li B, Liu Z and Wang W 2016 High electrical conductivity in oxygen deficient $BaSnO_3$ films *J. Alloys Compd.* **655** 389–94
[17] Tiwari A and Wong M —S 2020 Role of oxygen partial pressure on structure and properties of sputtered transparent conducting films of La-doped $BaSnO_3$ *Thin Solid Films* **703** 137986
[18] Li B, Liu Q, Zhang Y, Liu Z and Geng L 2016 Highly conductive Nb doped $BaSnO_3$ thin films on MgO substrates by pulsed laser deposition *J. Alloys Compd.* **680** 343–9
[19] Luo B C, Zhang J, Wang J and Ran P X 2015 Structural, electrical and optical properties of lanthanum-doped barium stannate *Ceram. Int.* **41** 2668–72
[20] Wang H F, Liu Q Z, Chen F, Gao G Y, Wu W and Chen X H 2007 Transparent and conductive oxide films with the perovskite structure: La- and Sb-doped $BaSnO_3$ *J. Appl. Phys.* **101** 106105
[21] Liu Q, Dai J, Li H, Li B, Zhang Y, Dai K and Chen S 2015 Optical and transport properties of Gd doped $BaSnO_3$ epitaxial films *J. Alloys Compd.* **647** 959–64
[22] Cava R J, Gammel P, Batlogg B, Krajewski J J, Peck W F Jr, Rupp L W Jr, Felder R and van Dover R B 1990 Nonsuperconducting $BaSn_{1-x}Sb_xO_3$. The 5s-orbital analog of $BaPb_{1-x}Bi_xO_3$, *Phys. Rev. B* **42** 4815–8
[23] Yamashita D, Takefuji S, Tsubomoto M and Yamamoto T 2010 Electronic structure analysis of Sb-doped $BaSnO_3$ *Mater. Sci. Eng. B* **173** 33–6
[24] Lu W, Jiang S, Zhou D and Gong S 2000 Structural and electrical properties of $Ba(Sn,Sb)O_3$ electroceramics materials *Sens. Actuators* **80** 35–7
[25] Vukašinović J *et al* 2020 The structural, electrical and optical properties of spark plasma sintered $BaSn_{1-x}Sb_xO_3$ ceramics *J. Eur. Ceram. Soc.* **40** 5566–75
[26] Yasukawa M, Kono T, Ueda K, Yanagi H and Hosono H 2010 High-temperature thermoelectric properties of La-doped $BaSnO_3$ ceramics *Mater. Sci. Eng. B* **173** 29–32
[27] Gupta A K and Sil A 2020 Phase composition and dielectric properties of spark plasma sintered $PbZr_{0.52}Ti_{0.48}O_3$ *Mater. Res. Express* **7** 036301

[28] Bell J G, Graule T and Stuer M 2022 Tuning of the microstructural and electrical properties of undoped $BaTiO_3$ by spark plasma sintering *Open Ceramics* **9** 100244
[29] Cho H J, Onozato T, Wei M, Sanchela A and Ohta H 2019 Effects of vacuum annealing on the electron mobility of epitaxial La-doped $BaSnO_3$ films *APL Mater.* **7** 022507
[30] Van Rossum G and Drake F L Jr 1995 Python reference manual *Centrum voor Wiskunde en Informatica Amsterdam* https://ir.cwi.nl/pub/5008
[31] Mathewson A G 1987 The effect of cleaning and other treatments on vacuum properties of technological materials used in ultrahigh vacuum *CERN-LEP-VA/87* **63** https://cds.cern.ch/record/183509/files/198801025.pdf
[32] Kumar U, Ansaree M J, Verma A K, Upadhyay S and Gupta G 2017 Oxygen vacancy induced electrical conduction and room temperature, ferromagnetism in system $BaSn_{1-x}Ni_xO_3$ ($0 \leqslant x \leqslant 0.20$) *Mater. Res. Express* 4116304
[33] Rajasekaran P, Arivanandhan M, Kumaki Y, Jayavel R, Hayakawa Y and Shimomura M 2020 Facile synthesis of morphology-controlled La:$BaSnO_3$ for the enhancement of thermoelectric power factor *CrystEngComm* **22** 5363–74
[34] Iftekhar Jaim H M, Lee S, Zhang X and Takeuchi I 2017 Stability of the oxygen vacancy induced conductivity in $BaSnO_3$ thin films on $SrTiO_3$ *Appl. Phys. Lett.* **111** 172102
[35] Miot C, Husson E, Proust C, Erre R and Coutures J P 1997 X-ray photoelectron spectroscopy characterization of barium titanate ceramics prepared by the citric route *Residual carbon study, J. Mater. Res.* **12** 2388–92
[36] Rajasekaran P, Kumaki Y, Arivanandhan M, Ibrahim Khaleeullah M M S, Jayavel R, Nakatsugawa H, Hayakawa Y and Shimomura M 2020 Effect of Sb substitution on structural, morphological and electrical properties of $BaSnO_3$ for thermoelectric application *Physica B* **597** 412387
[37] Dupin J-C, Gonbeau D, Vinatier P and Levasseur A 2000 Systematic XPS studies of metal oxides, hydroxides and peroxides *Phys. Chem. Chem. Phys.* **2** 1319È1324
[38] De Bièvre P and Taylor P D P 1993 table of the isotopic compositions of the elements *Int. J. Mass Spectrom. Ion Processes* **123** 149–66
[39] Walker F W, Parrington J R and Feiner F 1989 *Nuclides and Isotopes* fourteenth ed. (San Jose, California: General Electric Company)
[40] Juraić K, Gracin D, Čulo M, Rapljenović Ž, Plaisier J R, Hodzic A, Siketić Z, Pavić L and Bohač M 2020 Origin of mangetotransport properties in APCVD deposited tin oxide thin films *Materials* **13** 5182
[41] Prins M W J, Grosse-Holz K-O, Cillessen J F M and Feiner L F 1998 Grain-boundary-limited transport in semiconducting SnO_2 thin films: Model and experiments *J. Appl. Phys.* **83** 888–93
[42] Hossain K M, Mitro S K, Hossain M A, Modak J K, Rasheduzzaman M and Hasan M Z 2021 Influence of antimony on the structural, electronic, mechanical, and anisotropic properties of cubic barium stannate *Mater. Today Commun.* **26** 101868